Thixotropic gravity currents

Duncan R. Hewitt

September 28, 2012

1 Introduction

Fluids that undergo reversible and time-dependent changes to their internal structure as a result of flow are called thixotropic. Specifically, the internal structure of a thixotropic fluid is broken down by the presence of flow, while in the absence of flow, the structure rebuilds, and the fluid is said to 'heal' over time. Typically, the break-down of structure is relatively rapid, while the rebuilding of structure is slow.

Thixotropic behaviour has been reported in a wide range of fluids [6, 18]. Industrial drilling fluids and cements, printing inks and paints, oils and grease, biological fluids (e.g. blood), and food products such as mayonnaise, yoghurt, and ketchup have all been shown to exhibit elements of thixotropy. More complex fluids, such as dry foams and granular media, also exhibit many of the same phenomena as thixotropic fluids [12]. In nature, mineral slurries and certain mud and clay suspensions are thixotropic: part of the motivation for this study comes from mudslides, in which large volumes of mud can suddenly become 'de-structured' and catastrophically fail.

Thixotropic fluids are most commonly colloidal suspensions, with a microstructure that exhibits weak attractive forces between particles: this leads to flocculation and 'structuring' in the fluid at rest, while flow-induced mechanical stresses can break down this structure. On a macro-scale, this behaviour can be described by variations in the fluid viscosity. Thixotropic fluids are, therefore, typically modelled with a non-Newtonian variable viscosity, which decreases dramatically in the presence of shear, but increases slowly when the fluid is at rest. This rheology gives rise to a variety of phenomena: variable yield-stress behaviour, hysteresis in the constitutive relationship, and 'jamming' or 'avalanching' in the fluid (see, e.g. [1, 7, 10, 19]). We will examine these features in this report.

There has been a relatively wide range of work presenting rheological measurements and models for thixotropic fluids (see section 2). However, there have been very few studies that incorporate this rheology into a physical scenario. In this report, we consider the flow of a finite shallow layer of thixotropic fluid down an inclined plane under the action of gravity. Such a system has been well studied in the case of a Newtonian fluid [15, 16], and an ideal yield-stress (e.g. Bingham) fluid [4, 14, 17]. A previous study of a 'dam-break' of thixotropic fluid [8] has explored the gravity-driven flow of a (non-shallow) thixotropic fluid by tracking characteristics. There are, however, currently no systematic studies of the shallow thixotropic gravity current on a slope. Brief experimental observations of such a system by Coussot *et al.* [10], using bentonite clay, have suggested that this system can exhibit dramatic 'avalanche' behaviour: they found that fluid inclined at a certain angle

will not move at all, while fluid inclined at a slightly larger angle will dramatically collapse and flow rapidly down the inclined plate. In the latter case, they observed that a structured 'horseshoe' of fluid at the back of the current remained immobile, while the front of the current flowed down the slope. In the present study, we attempt to reproduce and explore such behaviour experimentally, and to describe it theoretically and numerically.

The report is structured as follows. In section 2, we discuss the rheological model of thixotropy that we will employ, including our simplifying 'rapid-transit' approximation. In section 3, we outline the governing equations for flow in a shallow layer (directly following [2]). In section 4, we present numerical results of the system, in both two and three dimensions, and discuss the main qualitative features of the flow. In section 5, we examine the stability of the system, and show that the flow is unstable to a form of interfacial instability. In general, this instability is relatively benign, in that it does not significantly destabilise the flow. Finally, in section 6 we present experimental results of the system using two different thixotropic fluids: a bentonite clay solution, and Heinz tomato ketchup. Broadly speaking, the experimental results show good qualitative agreement both with previously published observations [10], and with our numerical simulations.

2 Thixotropic model

2.1 Basic rheological model

A range of rheological models that describe the effects of thixotropy have been proposed (see, e.g. [6, 18]). Many of these models employ a time-dependent *structure parameter* $\lambda(t)$ to describe the amount of internal structure in the fluid [1, 10, 13, 19, 21]. The viscosity $\mu(\lambda)$ is then given as a prescribed function of the structure parameter. The constitutive equation for such a fluid, which relates the deviatoric stress tensor τ_{ij} to the rate of strain tensor $\dot{\gamma}_{ij}$, is given by the generalised Newtonian form,

$$\tau_{ij} = \mu[\lambda(t)]\,\dot{\gamma}_{ij}. \tag{1}$$

In this report, we use a rheological model of this form, which is outlined and discussed below. Our model is adapted from models presented by Coussot *et al.* [10, 11] and by Moller *et al.* [19, 20]. The main difference in our model is the (implicit) inclusion of an 'absolute yield stress', above which the fluid will flow irrespective of its structure: this removes an unphysical feature of the previous models, namely that infinite-viscosity fluid remains so for arbitrarily large stresses.

The structure parameter lies in the range $0 \leqslant \lambda \leqslant 1$: $\lambda = 1$ corresponds to fully structured fluid, and $\lambda < 1$ corresponds to fluid that is de-structured to some degree. The structure parameter is assumed to satisfy an evolution equation of the form

$$\frac{D\lambda}{Dt} = \frac{1-\lambda}{T} - \alpha\lambda\dot{\gamma}, \tag{2}$$

where $\dot{\gamma} = \sqrt{\dot{\gamma}_{ij}\dot{\gamma}_{ij}/2}$ is the second invariant of the rate of strain tensor $\dot{\gamma}_{ij}$, $T > 0$ is the constant 'healing timescale' for the fluid, and $\alpha > 0$ is a constant that controls the de-structuring of the fluid by the flow. The two terms on the right-hand side of (2) correspond, respectively, to the rebuilding or 'healing' of the fluid structure at rest, and the destruction

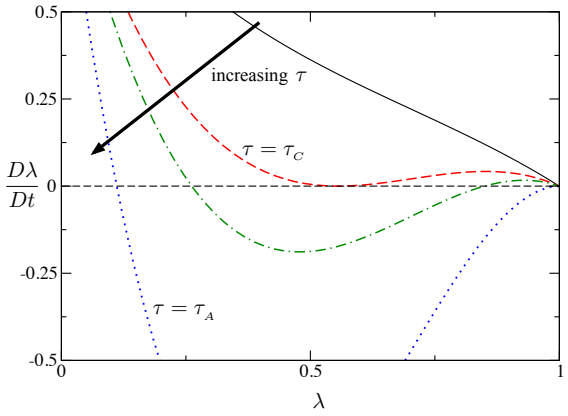

Figure 1: Phase diagram for λ, given by (4), for $\Gamma = 20$, $\beta = 0.9$, and increasing values of the stress τ as marked. There is a bifurcation at the critical value $\tau_C = 4\beta/\Gamma$: below this stress, the only fixed point is at $\lambda = 1$, which is stable, and corresponds to the structured state; above this stress there are two additional fixed points $\lambda_1 < \lambda_2 < 1$, the lower of which is stable. At a higher stress $\tau = \tau_A = 1/\Gamma(1-\beta)$, the unstable fixed point (λ_2) reaches $\lambda = 1$, and the fixed point at $\lambda = 1$ becomes unstable.

of structure by gradients in the flow. Empirical measurements [1, 7, 11, 20] suggest that both T and α are typically large, such that destruction of structure is fairly rapid, while regeneration of structure is very slow.

The structure parameter is related to the viscosity through an equation of the form

$$\mu = \frac{\mu_0 \dot{\gamma}^{n-1}}{(1-\lambda)^m (1-\beta\lambda)}, \tag{3}$$

where μ_0 is a constant reference viscosity, and $m \geqslant 1$, n, and $0.5 < \beta < 1$ are constant parameters. The viscosity increases with the structure λ, and diverges as the fluid becomes fully structured ($\lambda \to 1$). Therefore, if the fluid is fully structured, the constitutive equation (1) implies that the strain rate $\dot{\gamma}$ is zero.

Throughout this report, for simplicity, we take the parameters $m = n = 1$, such that the viscosity does not explicitly depend on the rate of strain $\dot{\gamma}$. The model can be generalised to give shear thinning or thickening behaviour (by changing n), or to give a different sensitivity of the viscosity on the structure (by changing m).

The evolution equation for λ (2) can be re-written in terms of the second invariant of the stress $\tau = \sqrt{\tau_{ij}\tau_{ij}/2}$, using the constitutive equation (1) and the viscosity equation (3) (here with $n = m = 1$), which gives

$$T\frac{D\lambda}{Dt} = (1-\lambda)\left[1 - \Gamma\lambda(1-\beta\lambda)\,\tau\right], \tag{4}$$

where $\Gamma = \alpha T/\mu_0$.

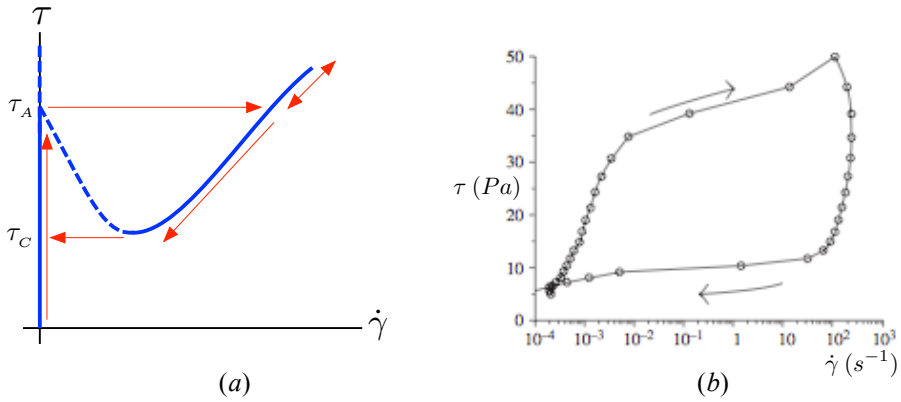

Figure 2: Constitutive relationships (1), showing the stress τ against the rate of strain $\dot{\gamma}$: (a) schematic of the model relationship at the steady-state solutions of (4) (thick blue), where dashed lines correspond to unstable fixed points, and the thin red arrows signify the 'rapid-transit' (see section 2.3) hysteresis behaviour that might be expected in a stress-ramp test; (b) measurements of 10 wt% bentonite clay under an increasing and decreasing stress-ramp test, taken from [19].

2.2 Implications of the model

The phase diagram for λ from (4) is shown in figure 1. For sufficiently small values of the stress, there is only one fixed point in the range $0 \leqslant \lambda \leqslant 1$, which is stable, and located at $\lambda = 1$. Therefore, if the stress is sufficiently small, the fluid always evolves towards the fully structured state. However, at the *critical stress* $\tau = \tau_{_C} = 4\beta/\Gamma$, there is a bifurcation at $\lambda = \lambda_{_C} = 1/2\beta$, and two additional fixed points $\lambda_{1,2}$ are created:

$$\lambda_{1,2} = \frac{1}{2\beta}\left[1 \mp \left(1 - \frac{4\beta}{\Gamma\tau}\right)^{1/2}\right]. \tag{5}$$

The lower value, λ_1, is a stable fixed point, which decreases as τ increases, while λ_2 is unstable and increases with τ. As the stress is increased further and reaches the *absolute stress* $\tau = \tau_{_A} = 1/\Gamma(1-\beta)$, this unstable fixed point λ_2 reaches $\lambda = 1$, and so, for $\tau > \tau_{_A}$, the fixed point at $\lambda = 1$ becomes unstable. Therefore, if the applied stress is very large, the fluid always evolves towards a de-structured state, corresponding to a small value of λ.

For a given value of the structure λ, there is a corresponding viscosity $\mu(\lambda)$, given by (3), which defines a relationship between the stress τ and the rate of strain $\dot{\gamma}$, given by the constitutive equation (1). This relationship is plotted schematically for the fixed points of (4) in figure 2(a). As discussed above, we can see that for small values of the stress $\tau < \tau_{_C}$, the fluid will evolve to the structured state with $\dot{\gamma} = 0$ ($\lambda = 1$). For large stress $\tau > \tau_{_A}$, the fluid will evolve to a de-structured state, with $\dot{\gamma} > 0$ ($\lambda \ll 1$).

For intermediate values of the stress $\tau_{_C} < \tau < \tau_{_A}$, the behaviour of the fluid will depend on the stress history of the sample: in other words, it will depend on which side of the unstable fixed point the structure parameter currently lies. The system therefore exhibits hysteresis, as can be seen by considering a simple stress-ramp experiment. Suppose the

fluid is initially fully structured, and a gradually increasing stress is applied. The shear rate will remain zero until the stress exceeds the absolute stress, $\tau > \tau_{_A}$. At this point, the fluid will 'de-structure', λ will decrease towards the small stable fixed point, and $\dot{\gamma}$ will increase towards the stable branch. If the stress is then decreased, the strain rate will remain on the stable (non-zero) branch until the stress falls below $\tau_{_C}$, at which point the structure parameter will evolve back towards $\lambda = 1$, and the shear rate will decay to zero. Experimental results of such a test on bentonite clay are shown in figure 2(b).

It should be noted that if the fluid is not initially fully structured, such that $\lambda < 1$, then the corresponding initial viscosity $\mu_{_I}$ has some finite value. Alternatively, the viscosity of a real fluid is unlikely to be unbounded, in which case $\mu_{_I}$ represents the upper bound that can be attained. In either case, we would not expect the rate of strain to remain zero as the stress is increased: instead it should follow the linear constitutive relationship $\tau = \mu_{_I}\,\dot{\gamma}$. The corresponding stress at which the fluid evolves to the 'de-structured' small-λ stable branch would then be smaller than $\tau_{_A}$, and the effects of hysteresis would be smaller. This behaviour can be seen in the experimental measurements of figure 2(b), where the initial slope of the curve is not vertical.

The extent of hysteresis in the system is controlled by the parameter β. As the value of β is increased towards 1, the value of $\tau_{_A}$ increases towards ∞, while $\tau_{_C}$ remains finite: the size of the hysteresis loop therefore increases. Alternatively, as β is decreased towards $1/2$, $\tau_{_A} \to \tau_{_C}$, and there is no hysteresis in the system. On setting $\beta = 0$ and ignoring the time derivative in (4), this thixotropic rheology reduces to that for an ideal Bingham yield-stress fluid, with yield stress $1/\Gamma$.

It is worth, at this point, drawing a comparison between this thixotropic model (for non-zero β) and models for ideal yield-stress fluids (i.e. Bingham or Herschel–Buckley models [3]). The thixotropic model does incorporate the idea of a yield stress, as for stresses below $\tau_{_C}$ the strain rate always evolves to zero. However, there are some significant differences. Firstly, in the thixotropic model the value of the 'yield stress' is dependent on the stress history of the particular fluid element: the system exhibits hysteresis, and the extent of the hysteresis loop in the constitutive relationship is given by the extent to which the fluid is structured at that particular time. In contrast, in an ideal yield-stress fluid the yield stress is constant. Secondly, in the thixotropic model there is a discontinuity in the steady-state rate of strain at the 'yield stress', which has been described as a 'viscosity bifurcation' [11]: the viscosity, which is infinite for smaller stresses, discontinuously becomes finite and relatively small as the stress is increased past the 'yield stress'. In an ideal yield-stress fluid, however, the viscosity varies continuously away from infinity as the stress is increased past the yield stress. A more detailed discussion of the differences between thixotropic models of this form and yield-stress models can be found in [20]. In sections 4 and 6, we will compare the behaviour of thixotropic and ideal yield-stress fluids numerically and experimentally, and show that there are significant phenomenological differences between the two types of fluid.

2.3 Rapid-transit

Rheological measurements and observations of a variety of thixotropic fluids [1, 7, 11, 20] have shown that there is a significant separation of timescales between the 'healing' time T,

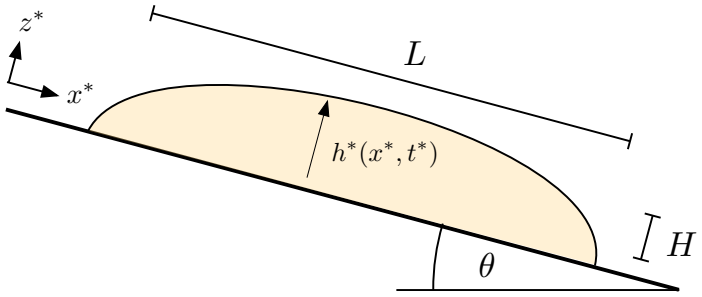

Figure 3: Schematic showing the system under consideration: fluid of aspect ratio $\varepsilon = H/L \ll 1$ on a slope of angle θ, in two dimensions.

which is typically large, and the timescale over which the fluid evolves to the steady state under stress, which is often much smaller. Motivated by these observations, we make a simplifying 'rapid-transit' approximation to the evolution equation for λ (4): the evolution to the steady state is assumed to be instantaneous, and the material derivative is replaced by zero. Equation (4) therefore becomes

$$(1-\lambda)\left[1-\Gamma\lambda\left(1-\beta\lambda\right)\tau\right]=0. \tag{6}$$

The relevant root λ of (6) for a given stress τ is determined by the stability of the full time-dependent equation (4).

The constitutive relationship (1) is then given exactly by the steady-state curve plotted in figure 2(a). At the bifurcation points $\tau = \tau_{_C}$ and $\tau = \tau_{_A}$, the structure parameter jumps to the structured ($\lambda = 1$, $\dot{\gamma} = 0$) or de-structured ($\lambda \ll 1$, $\dot{\gamma} > 0$) branches, as shown by the arrows in figure 2(a). For intermediate values of the stress $\tau_{_C} < \tau < \tau_{_A}$, the corresponding value of λ depends on the stress history of the fluid.

3 Gravity driven flow in a shallow layer

In this study, we incorporate the rheological 'rapid-transit' thixotropic model into the problem of shallow fluid flow on an inclined plane. In order to distinguish between dimensional and dimensionless variables, in this section we denote all dimensional quantities with a *. The problem formulation is independent of the rheology, and exactly follows that given in [2].

3.1 Dimensional formulation

We consider the flow (u^*, w^*) of a finite volume of fluid of density ρ, in two dimensions (x^*, z^*), where the x^*-axis is aligned along a slope inclined at a constant angle θ to the horizontal. The fluid lies in a shallow layer, such that the typical depth scale H is much smaller than the typical along-slope scale L. We define their ratio to be $\varepsilon = H/L \ll 1$. The fluid has depth $z^* = h^*(x^*, t^*)$, as shown in figure 3.

The flow is incompressible,

$$\frac{\partial u^*}{\partial x^*} + \frac{\partial w^*}{\partial z^*} = 0, \tag{7}$$

and satisfies the Cauchy momentum equations,

$$\rho\left(\frac{\partial u^*}{\partial t^*}+u^*\frac{\partial u^*}{\partial x^*}+w^*\frac{\partial u^*}{\partial z^*}\right)=\rho g\sin\theta-\frac{\partial p^*}{\partial x^*}+\frac{\partial \tau^*_{xz}}{\partial z^*}+\frac{\partial \tau^*_{xx}}{\partial x^*}, \tag{8}$$

$$\rho\left(\frac{\partial w^*}{\partial t^*}+u^*\frac{\partial w^*}{\partial x^*}+w^*\frac{\partial w^*}{\partial z^*}\right)=-\rho g\cos\theta-\frac{\partial p^*}{\partial z^*}+\frac{\partial \tau^*_{xz}}{\partial x^*}+\frac{\partial \tau^*_{zz}}{\partial z^*}. \tag{9}$$

The deviatoric stress tensor τ^*_{ij} is related to the rate of strain tensor $\dot{\gamma}^*_{ij}$ by the constitutive equation (1). The boundary conditions are given by no normal or tangential flow at the base,

$$u^*=w^*=0 \qquad \text{at} \qquad z^*=0, \tag{10}$$

no normal stress at the upper boundary,

$$\left(\tau^*_{ij}-p^*\delta_{ij}\right)n_j=0 \quad \text{at} \quad z^*=h^*(x^*,t^*), \tag{11}$$

and the kinematic condition at the upper boundary,

$$\frac{\partial h^*}{\partial t^*}+u^*\frac{\partial h^*}{\partial x^*}-w^*=0 \quad \text{at} \quad z^*=h^*(x^*,t^*), \tag{12}$$

where $\boldsymbol{n}\propto(-h^*_{x^*},1)$ is a vector that is normal to the surface $z^*=h^*$. The kinematic condition (12), combined with the continuity equation (7), gives

$$\frac{\partial h^*}{\partial t^*}+\frac{\partial}{\partial x^*}\int_0^{h^*}u^*\,\mathrm{d}z^*=0. \tag{13}$$

3.2 Dimensionless formulation

We scale x^* with L, z^* with H, and the pressure p^* with $\rho gH\cos\theta$. We take a constant velocity scale U, and scale u^* with U, w^* with HU/L, and time t^* with L/U. The stress τ^*_{ij} is scaled with μ_0U/H. We assume that the horizontal pressure gradients balance the vertical gradients of the shear stress, and thus identify $U=H^3g\cos\theta/L\mu_0$.

As discussed above, we define the ratio $H/L=\varepsilon\ll1$. With respect to dimensionless variables, (8), (9), and (13) are given by

$$\varepsilon^2Re\left(\frac{\partial u}{\partial t}+u\frac{\partial u}{\partial x}+w\frac{\partial u}{\partial z}\right)=S-\frac{\partial p}{\partial x}+\frac{\partial \tau_{xz}}{\partial z}+\varepsilon\frac{\partial \tau_{xx}}{\partial x}, \tag{14}$$

$$\varepsilon^4Re\left(\frac{\partial w}{\partial t}+u\frac{\partial w}{\partial x}+w\frac{\partial w}{\partial z}\right)=-1-\frac{\partial p}{\partial z}+\varepsilon^2\frac{\partial \tau_{xz}}{\partial x}+\varepsilon\frac{\partial \tau_{zz}}{\partial z}, \tag{15}$$

$$\frac{\partial h}{\partial t}+\frac{\partial}{\partial x}\int_0^h u\,\mathrm{d}z=0, \tag{16}$$

where $S=\varepsilon^{-1}\tan\theta$, and the Reynolds number Re is given by $Re=\rho UL/\mu_0$. The components of the rate of strain tensor are given by

$$\dot{\gamma}_{xx}=-\dot{\gamma}_{zz}=2\varepsilon\frac{\partial u}{\partial x}, \qquad \dot{\gamma}_{xz}=\frac{\partial u}{\partial z}+\varepsilon^2\frac{\partial w}{\partial x}. \tag{17}$$

The stress boundary condition (11) becomes

$$\begin{pmatrix}\varepsilon\tau_{xx}-p & \varepsilon\tau_{xz}\\ \varepsilon\tau_{xz} & -\varepsilon\tau_{xx}-p\end{pmatrix}\begin{pmatrix}-\varepsilon\partial h/\partial x\\ 1\end{pmatrix}=\mathbf{0} \quad \text{at} \quad z=h(x,t); \tag{18}$$

3.3 Leading order equations

Under the assumption that $S \sim O(1)$ and Re is no larger than $O(1/\varepsilon)$, the leading order terms in ε from (14) and (15) give

$$0 = S - \frac{\partial p}{\partial x} + \mu \frac{\partial^2 u}{\partial z^2}, \tag{19}$$

$$0 = -1 - \frac{\partial p}{\partial z}. \tag{20}$$

Together with the leading order boundary conditions from (11), equations (19) and (20) give

$$p = h - z, \tag{21}$$

$$\tau_{xz} = \mu \frac{\partial u}{\partial z} = \left(S - \frac{\partial h}{\partial x} \right) (h - z). \tag{22}$$

If the viscosity μ is a constant, (16) and (22) can be combined, and reduce to the usual governing equation for a Newtonian viscous gravity current on a slope [16]. Here, instead, the viscosity is given as a function of the structure parameter λ (3), and the structure parameter $\lambda(\tau)$ is given by the rapid transit model, discussed in section 2.3. These equations are given here in dimensionless form:

$$\mu(\lambda) = \frac{1}{(1-\lambda)(1-\beta\lambda)}, \tag{23}$$

$$(1-\lambda)\left[1 - \Gamma\lambda(1-\beta\lambda)|\tau_{xz}|\right] = 0, \tag{24}$$

where we have set the parameters $n = m = 1$, rescaled the parameter Γ as $\Gamma = \alpha T/\varepsilon$, and replaced the stress τ by $|\tau_{xz}|$ following (17). Since we expect α and T to be large, we also typically consider Γ to be large.

3.4 Anatomy of the flow

Before we present our numerical results, it will be helpful to examine the anatomy of the flow, which is shown schematically in figure 4. From the rheological model, and the hysteresis behaviour shown in figure 2, we should expect changes in the fluid structure, and thus changes in the flow, at the bifurcation stresses: that is, at the critical and absolute values of the stress, $\tau_{_C}$ and $\tau_{_A}$. In the shallow-layer formulation, the stress is dominated by the shear stress τ_{xz}, which is given by (22), and is a linearly decreasing function of z. The contour $\tau = \tau_{_C}$ therefore defines a surface $z(\tau_{_C}) \leqslant h$. Above this surface, the stress is less than the critical value, and, as such, the fluid is structured: $\lambda = 1$, and $\dot{\gamma} = \partial u/\partial z = 0$.

Similarly, the contour $\tau = \tau_{_A}$ defines a surface $z(\tau_{_A}) \leqslant z(\tau_{_C})$. Below this surface, the stress is greater than the absolute value, and the fluid is de-structured: therefore $\lambda \ll 1$, and $\partial u/\partial z > 0$.

Between the two stress surfaces, $z(\tau_{_C}) < z < z(\tau_{_A})$, the structure of the flow depends on the history of each fluid element. Suppose that the fluid is initially fully structured. Then, when the fluid is inclined, the de-structured fluid will be exactly bounded above by the absolute stress surface $z = z(\tau_{_A})$. However, as the flow evolves, de-structured fluid

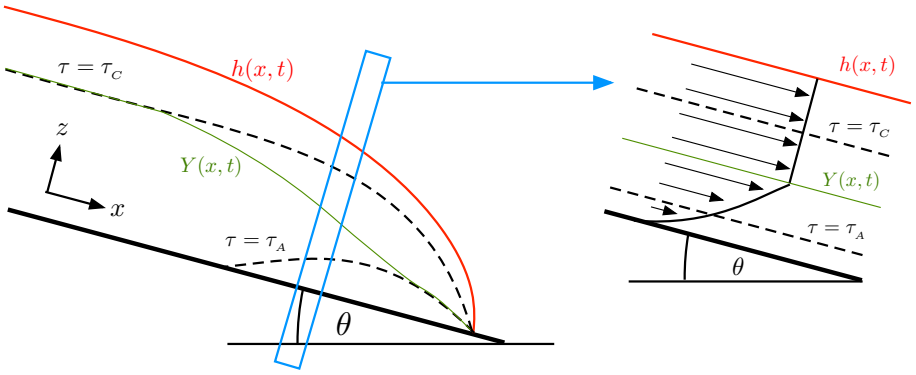

Figure 4: Schematic showing the flow of thixotropic fluid down a slope of angle θ. The height $h(x,t)$ is shown in red. Lines of constant shear stress $\tau{=}\tau_A$ and $\tau{=}\tau_C$ are shown dashed. Above the line $\tau = \tau_C$, the fluid is fully structured and $\lambda = 1$, while below the line $\tau = \tau_A$, the fluid is de-structured and $\lambda \ll 1$. The yield surface $z = Y(x,t)$ (green), which separates structured and de-structured flow, is bounded by these stress contours. Between the two contours, the structure of the flow is determined by the local stress history: in this region the yield surface is a material curve which satisfies (26). The inset shows a typical velocity profile $u(z)$ through a slice of the flow as marked: $u(z)$ increases from zero at the base up to the yield surface, at which point there is a discontinuity in $\partial u/\partial z$, and plug flow in the structured region above the yield surface.

elements will remain de-structured until the stress falls below the critical stress τ_C. These fluid elements will also move with the flow, and so there is a material curve which runs between the two stress contours, and separates the structured and de-structured fluid.

We can, therefore, define a yield surface $z = Y(x,t)$ which runs throughout the current and separates the structured fluid above from the de-structured fluid below (figure 4). At points in the flow where the absolute stress surface $z(\tau_A)$ is moving up into structured fluid, the yield surface lies along this stress surface. Similarly, at points in the flow where the critical stress surface is moving down into de-structured fluid, the yield surface lies along this stress surface. Between the two stress surfaces, the yield surface is a material curve, as discussed above. Therefore, in this region $z(\tau_C) < z < z(\tau_A)$ the yield surface satisfies a kinematic condition,

$$\frac{\partial Y}{\partial t} + u\frac{\partial Y}{\partial x} - w = 0 \qquad \text{on} \qquad z = Y(x,t), \tag{25}$$

which, together with incompressibility (7), reduces to an evolution equation for Y in this region:

$$\frac{\partial Y}{\partial t} + \frac{\partial}{\partial x}\int_0^Y u \,\mathrm{d}z = 0. \tag{26}$$

For clarity, a summary of our complete model is given here. The leading-order stress contribution (22) and the rheological model (23), (24), are given by

$$\tau_{xz} = \mu(\lambda)\frac{\partial u}{\partial z} = \left(S - \frac{\partial h}{\partial x}\right)(h - z)\,, \tag{27}$$

$$\mu(\lambda) = \frac{1}{(1-\lambda)\,(1-\beta\lambda)}, \tag{28}$$

$$(1-\lambda)\,[1-\Gamma\lambda\,(1-\beta\lambda)\,|\tau_{xz}|] = 0. \tag{29}$$

The relevant root $0 \leqslant \lambda \leqslant 1$ of (29) is given by the stability of the full time-dependent equation (4). Equations (27)—(29) are solved together with the evolution equation (16) for the height of the current $h(x,t)$,

$$\frac{\partial h}{\partial t} + \frac{\partial}{\partial x}\int_0^h u\,\mathrm{d}z = \frac{\partial h}{\partial t} + \frac{\partial}{\partial x}\int_0^Y (h-z)\,\frac{\partial u}{\partial z}\,\mathrm{d}z = 0. \tag{30}$$

The location of the yield surface $Y(x,t)$ depends on the stress history of the fluid. In regions where the absolute stress surface $z(\tau_{_A})$ is moving up into structured fluid, or where the critical stress surface $z(\tau_{_C})$ is moving down into de-structured fluid, the yield surface $Y(x,t)$ lies along the respective stress surface (figure 4). Otherwise, the yield surface lies between the two stress surfaces and evolves as a material curve (26):

$$\frac{\partial Y}{\partial t} + \frac{\partial}{\partial x}\int_0^Y u\,\mathrm{d}z = \frac{\partial Y}{\partial t} + \frac{\partial}{\partial x}\int_0^Y (Y-z)\,\frac{\partial u}{\partial z}\,\mathrm{d}z = 0. \tag{31}$$

4 Numerical results

4.1 Initial conditions

The initial height profile $h(x, t=0)$ for our numerical calculations is given by the final rest state of a finite volume of fluid that has slumped under gravity on a horizontal plate. This state corresponds to one in which the stress in the current has fallen below the critical stress $\tau_{_C}$ at all points: the fluid then becomes structured and stops flowing.

Applying this stress condition at $z = 0$, (27) (with $S = 0$) gives a simple differential equation for the height of the final state on a horizontal plate,

$$\left|h\frac{\partial h}{\partial x}\right| = \tau_{_C} = \frac{4\beta}{\Gamma}. \tag{32}$$

Equation (32) can be combined with a volume-conservation condition, and solved to give a profile (centred on $x = 0$)

$$h(x) = \left[\left(\frac{6\beta V}{\Gamma}\right)^{2/3} - \frac{8\beta}{\Gamma}\,|x|\right]^{1/2}, \tag{33}$$

where V is the constant volume of fluid. Equation (33) is identical to the final state obtained for an ideal yield-stress fluid with yield stress $\tau_{_C}$. This final state is then used as an initial condition in the numerical calculations. In addition, in these simulations we assume that the fluid which has attained this initial condition has then been left to rest on the horizontal plane for sufficient time that the initial structure has fully healed throughout the fluid, and is uniformly given by $\lambda = 1$.

4.2 Two-dimensional results

We have solved the governing equations (30)-(31) numerically. The calculations were significantly simplified by analytically integrating over the vertical component z in these equations using (27)-(29), and thus reducing the system to a one-dimensional model (these calculations result in fairly involved analytic expressions, which are not shown here). The resulting one-dimensional equations were solved numerically, using second-order centred finite differences in space, and a second-order midpoint method in time.

Numerical results for $\Gamma = 20$, $\beta = 0.95$, and $S = 1.5$ are shown in figure 5. In addition to the height of the interface $h(x,t)$, this figure shows the two stress surfaces and the yield surface that were discussed in section 3.4.

The initial stress on the fluid is greatest at the base, below the highest point of the current. Therefore, as fluid begins to move, the most significant de-structuring occurs there, and leads to a partial collapse of the fluid column above. This process results in the formation of a 'nose' at the front of the current (figures 5c and d). There is a local minimum in the height profile in the interior of the current, and, most notably, at the back of the current there is a raised remnant of structured fluid that remains immobile. In contrast, figure 5(e) also shows the evolution of an ideal Bingham yield-stress fluid, with a yield stress given by $\tau_{_A}$, and the same initial profile. Here, the height of the current has quite a different profile, being highest at the front, not having a height minimum in the middle of the current, and not leaving a raised remnant at the back, at least for the length of the computation shown.

Some notable oscillations can be observed in the results of figure 5. These features appear to take the form of high-wavenumber travelling waves, which are typically first observed on the material part of the yield surface $z = Y$ near to one of the stress contours. The waves are independent of the temporal resolution of the simulations, but do exhibit some dependence on the spatial resolution. However, the macro-scale features of the flow remain almost unaltered, as the waves move with the flow and are rapidly damped when the yield surface joins one of the two stress contours. In section 5, we rationalize these waves in the form of an instability of the material part of the yield surface.

4.2.1 Critical angle

The stress on the fluid increases with the slope S (27). If the slope is not sufficiently high, the stress will be below the absolute value $\tau_{_A}$ throughout the fluid. The fluid will therefore remain structured, and there will be no flow. However, if any of the fluid is de-stabilised, then it will remain destabilised until the stress on that fluid parcel falls below the critical value $\tau_{_C}$. We therefore find that there is a critical vale of S, corresponding to a critical angle, below which there is no flow, and above which the fluid will de-structure and flow. This behaviour agrees with the 'avalanching' above a critical angle, which was reported in [10].

The critical angle can be calculated analytically. The initial condition for the height of the current is given by $|h\partial h/\partial x| = \tau_{_C}$ (see section 4.1). For a given inclination angle, and thus a given value of S, the new stress along the base of the current is given by

$$\tau = \left| S - \frac{\partial h}{\partial x} \right| h = \tau_{_C} + Sh. \tag{34}$$

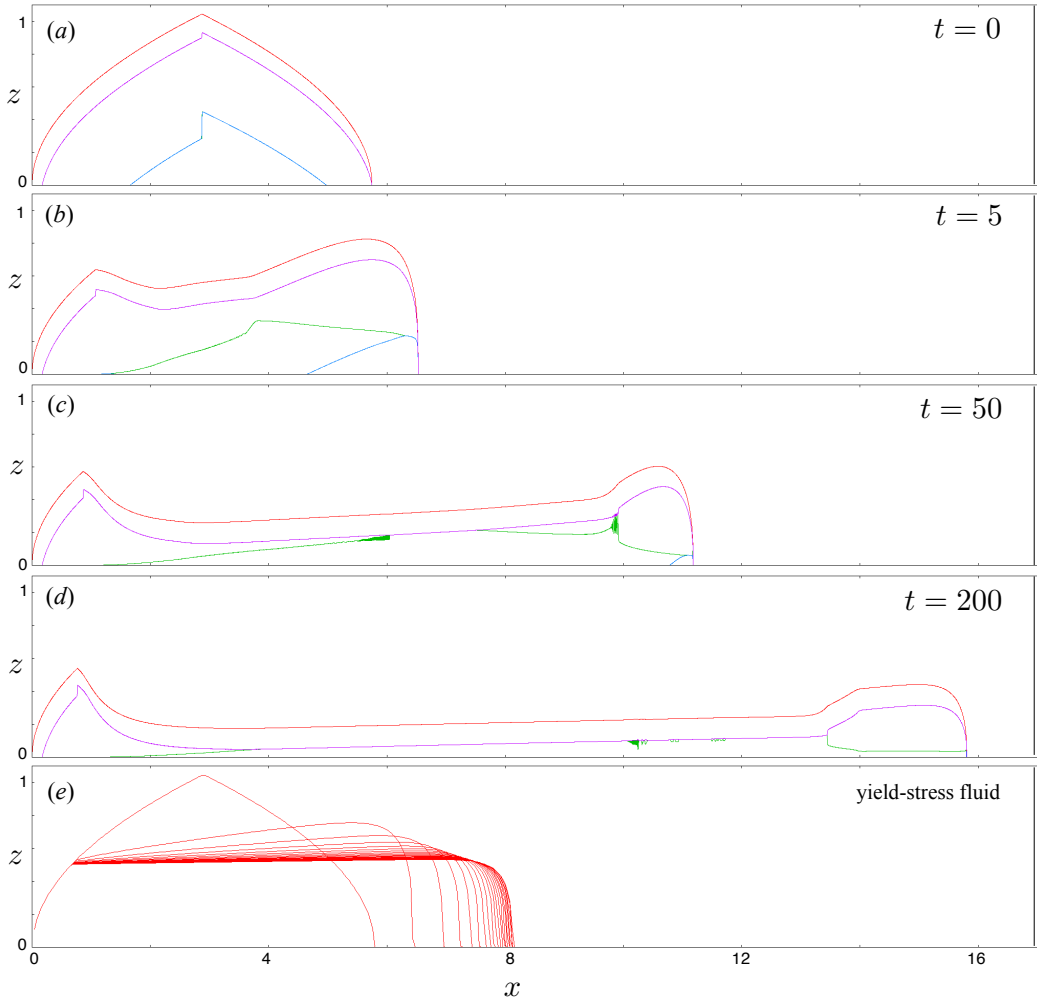

Figure 5: Numerical results of the two-dimensional system, for $\Gamma = 20$, $\beta = 0.95$, $S = 1.5$, and an initial volume of fluid $V = 4$. The lines show the height of the current $h(x,t)$ (red), the yield surface $Y(x,t)$ (green), the critical stress contour (purple), and the absolute stress contour (blue), at times: (a) $t = 0$; (b) $t = 5$; (c) $t = 50$; and (d) $t = 200$. For comparison, (e) shows the height of an ideal Bingham yield-stress fluid, with yield stress (Bingham number) τ_A, slope $S = 2$, and the same initial conditions as (a). The height profile in (e) is printed every 10 time units.

The fluid will de-structure if this stress exceeds the absolute value $\tau_{_A}$. Therefore, for a given initial height profile, the critical angle Θ is given by

$$S = \frac{\tan\Theta}{\varepsilon} = \frac{\tau_{_A} - \tau_{_C}}{\max_x h} = \frac{(1-2\beta)^2}{(6\beta\Gamma^2 V)^{1/3}(1-\beta)}, \tag{35}$$

where $\max_x h$ signifies the maximum value of h over all values of x, which we have substituted from the initial height profile (33), for a given constant volume of fluid V. We have also substituted the expressions for $\tau_{_A} = 1/\Gamma(1-\beta)$ and $\tau_{_C} = 4\beta/\Gamma$ from section 2.2.

4.2.2 Final rest state

As in the case on a horizontal plate (section 4.1), the final rest state for the current is given by the height profile that corresponds to the stress on the base falling below the critical value everywhere. After this point, the fluid re-structures and there is no further flow. Therefore the final state is identical to that for an ideal yield-stress fluid with a yield stress $\tau_{_C}$ [14], and is given by

$$\left| S - \frac{\partial h}{\partial x} \right| h = \tau_{_C}. \tag{36}$$

Equation (36) has a solution $h(x)$ that is given implicitly by

$$\log\left(1 - \frac{S}{\tau_{_C}}h\right) + \frac{S}{\tau_{_C}}h = \frac{S^2}{\tau_{_C}}(x - x_{_F}), \tag{37}$$

where $x_{_F}$ is a constant of integration corresponding to the final position of the nose of the current. If the back of the current has not moved from the initial state, then (37) is matched with the initial condition there, in such a way as to conserve volume. This matching determines $x_{_F}$. Equation (37) gives profiles for the height that are almost flat, with a localised steep drop at the nose. Therefore, perhaps surprisingly, the theory predicts that the raised structured remnant at the back of the current (figure 5) will eventually collapse to give a roughly flat end state. This end state is not attained until the stress on the fluid is everywhere below the critical stress, and numerical results suggest that the approach to this state is extremely slow compared with the initial rate of spreading of the current.

4.3 Three-dimensional results

We can also perform the analysis of section 3 for three-dimensional flow, which includes the cross-slope co-ordinate y and velocity v. The leading order equations (c.f. (27) and (30) in two dimensions) reduce to

$$\frac{\partial h}{\partial t} + \frac{\partial}{\partial x}\int_0^h u\,\mathrm{d}z + \frac{\partial}{\partial y}\int_0^h v\,\mathrm{d}z = 0, \tag{38}$$

$$\tau_{xz} = \mu(\lambda)\frac{\partial u}{\partial z} = \left(S - \frac{\partial h}{\partial x}\right)(h-z), \qquad \tau_{yz} = \mu(\lambda)\frac{\partial v}{\partial z} = -\frac{\partial h}{\partial y}(h-z), \tag{39}$$

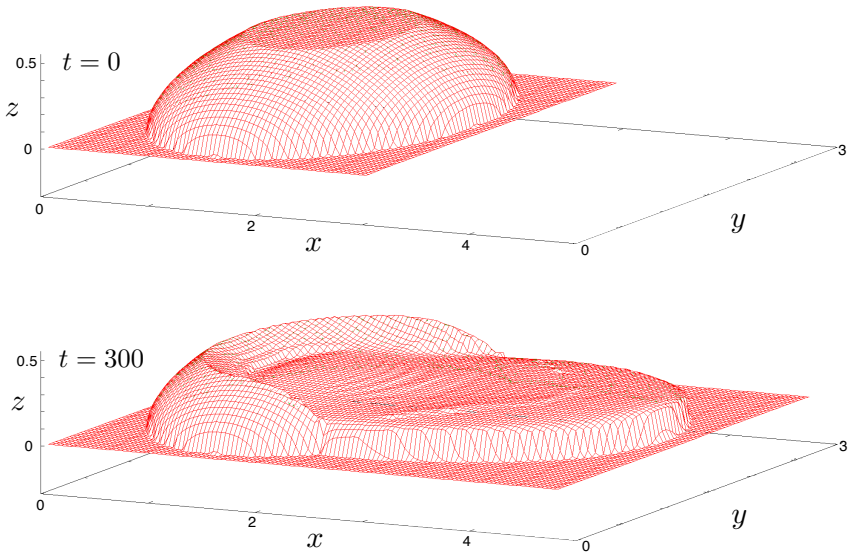

(*a*)

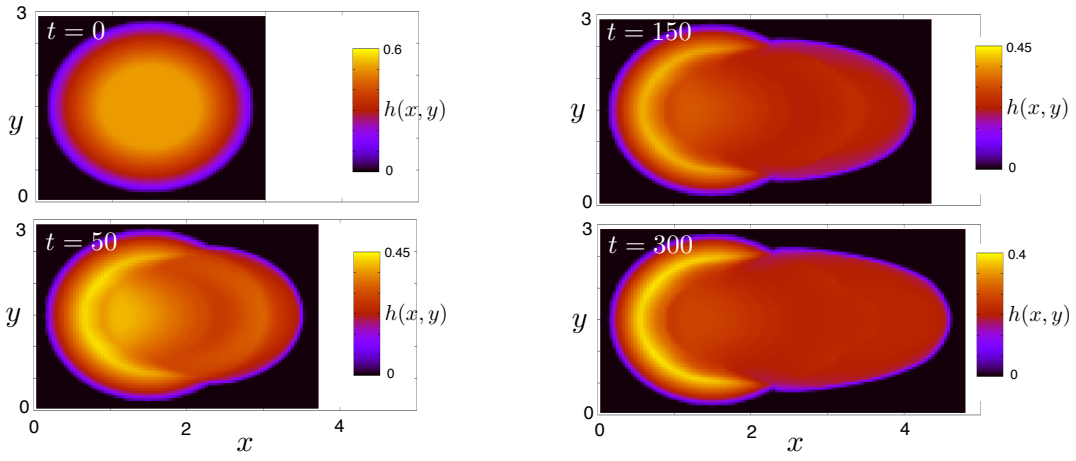

(*b*)

Figure 6: Numerical results of the three-dimensional system, for $\Gamma = 20$, $\beta = 0.9$, $S = 1$, and an initial volume of fluid $V = 2$: (a) the height of the current $h(x, y, t)$ visualised in three dimensions, for $t = 0$ and $t = 300$; (b) colour maps of the height of the current, viewed from above, for $t = 0$, $t = 50$, $t = 150$, and $t = 300$ as marked. A clear 'horseshoe' of structured fluid can be seen at the back of the current.

$$\tau = \sqrt{\tau_{xz}^2 + \tau_{yz}^2} = (h - z)\sqrt{\left(S - \frac{\partial h}{\partial x}\right)^2 + \left(\frac{\partial h}{\partial y}\right)^2}, \tag{40}$$

and the rapid-transit rheological model is the same as previously (28), (29).

As mentioned in section 4.2, we can calculate the integrals in the vertical component of (38) analytically (not shown here), and thus reduce the system to a two-dimensional model in x and y. We have solved (38)–(40) numerically, using a modification of the one-dimensional routine discussed in section 4.2.

Figure 6 shows solutions of the height $h(x, y, t)$ at different times, for $\Gamma = 20$, $\beta = 0.9$, and $S = 1$. Similar qualitative features to the two-dimensional model can be seen. Firstly, the fluid appears to collapse most rapidly in the centre. Secondly, a distinct remnant of structured fluid is left behind at the back of the current, which persists as the nose flows away down the slope. This structured remnant appears to be very similar to the observations of a 'horseshoe' that were reported in [10]. There is less of a distinct raised nose in these simulations as in the one-dimensional results (figure 5); this appears to be due to the lower value of β used here, which corresponds to a smaller hysteresis loop in the constitutive equation. At values of β closer to 1, the calculations show noticeable high-wavenumber oscillations in the material part of the yield surface $z = Y$, which are also visible as ripples in the free surface $z = h$: these are analogous to the features seen in the two-dimensional results, and are discussed in the following section. Their possible physical relevance is considered in the context of our experimental results with ketchup (section 6.2).

5 Stability

It has been shown that two inclined shallow layers of Newtonian [9] or non-Newtonian power-law [5] fluid with differing viscosities can be unstable to an interfacial instability, even in the absence of inertia, due to the additional degrees of freedom given by the material surface between the layers. We might, therefore, expect to find a similar interfacial instability in the shallow thixotropic layer, when the yield surface is a material curve which separates infinite-viscosity structured fluid above from relatively low-viscosity de-structured fluid below. Indeed, as mentioned in section 4, we can observe instabilities forming on the material yield surface in our numerical simulations.

In this section we consider the linear stability of an idealised two-dimensional system, in which the background height $z = h$ and yield surface $z = Y$ are both constant. The yield surface is a material curve lying between the two stress contours $\tau = \tau_A$ and $\tau = \tau_C$, as shown in figure 7(a). This study is limited to times before the yield surface touches either of these stress contours. We begin this section by performing a theoretical stability analysis, which shows that the system is always weakly unstable to perturbations at any wavenumber. We then present numerical simulations of the system, which reveal that the instability results in the generation of travelling shocks on the yield surface.

5.1 Theoretical stability analysis

The system is governed by continuity below and above the yield surface, and by the kinematic condition at both $z = Y$ and $z = h$. These conditions give governing equations (30)

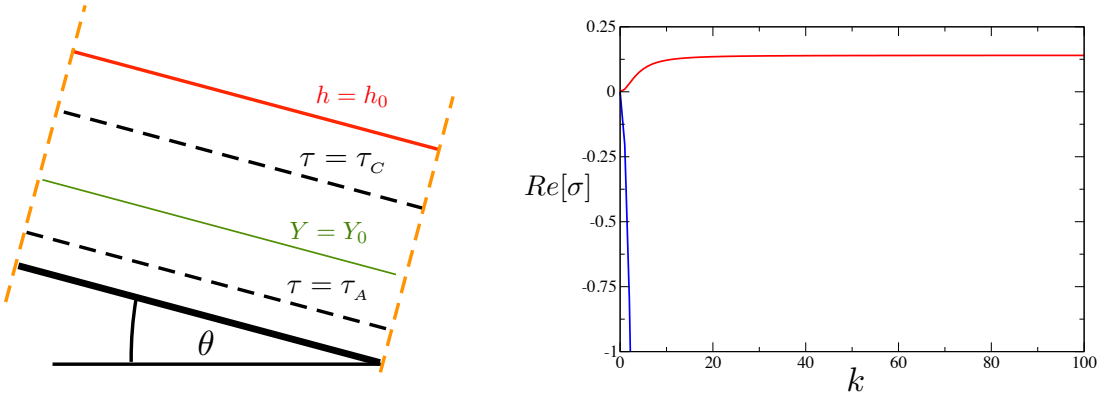

(*a*) (*b*)

Figure 7: (*a*) The system under consideration in the linear stability analysis: the background height and yield surface are given by the constants h_0 and Y_0 respectively, and, for the numerical calculations, the boundaries are periodic. (*b*) The two roots of the growth rate, for $\Gamma = 20$, $\beta = 0.95$, $S = 2$, $h_0 = 1$, $Y_0 = 0.25$. One root (blue) decays like $-k^2$; the other (red) tends to a small positive constant for large values of k.

and (31), which can be written in the form

$$\frac{\partial h}{\partial t} + \frac{\partial}{\partial x} F(h, Y) = 0, \qquad \frac{\partial Y}{\partial t} + \frac{\partial}{\partial x} G(h, Y) = 0. \tag{41}$$

The functions F and G are the fluxes of h and Y respectively, given by

$$F = \int_0^h u \, \mathrm{d}z = \int_0^Y (h - z) \frac{\partial u}{\partial z} \, \mathrm{d}z, \tag{42}$$

$$G = \int_0^Y u \, \mathrm{d}z = \int_0^Y (Y - z) \frac{\partial u}{\partial z} \, \mathrm{d}z. \tag{43}$$

The rate of strain $\partial u / \partial z$ (27) depends on the structure parameter λ, which itself is a function of the shear stress (29), and thus a function of z. The fluxes (42), (43) can therefore be written as

$$F(h, h_x, Y) = (S - h_x) \int_0^Y (h - z)^2 \, (1 - \lambda) \, (1 - \beta\lambda) \, \mathrm{d}z, \tag{44}$$

$$G(h, h_x, Y) = (S - h_x) \int_0^Y (h - z) \, (Y - z) \, (1 - \lambda) \, (1 - \beta\lambda) \, \mathrm{d}z, \tag{45}$$

where h_x is the partial derivative of h with respect to x, and, from (29), the structure parameter is given by

$$\lambda(z, h, h_x) = \frac{1}{2\beta} \left[1 - \left(1 - \frac{4\beta}{\Gamma \, (h - z) \, (S - h_x)} \right)^{1/2} \right]. \tag{46}$$

These integrals (44) and (45) can be calculated analytically (not shown here).

We perform a linear stability analysis of (41) by looking for normal modes, with growth rate σ and wavenumber k:

$$h = h_0 + \tilde{h}e^{\sigma t + ikx}, \qquad Y = Y_0 + \tilde{Y}e^{\sigma t + ikx}, \tag{47}$$

where h_0 and Y_0 are the constant background values of the height and the yield surface, and $\tilde{h}$ and $\tilde{Y}$ are small perturbations which satisfy $\tilde{h}$, $\tilde{Y} \ll h_0$, Y_0. Neglecting terms that are non-linear in the perturbation quantities, we find that the growth rate σ satisfies a dispersion relationship of the form

$$\sigma^2 + \sigma\left(Ak^2 + Bik\right) + Cik^3 + Dk^2 = 0 \tag{48}$$

where A, B, C, and D are real functions of the governing parameters of the problem, Γ, β, S, h_0, and Y_0, and are given in terms of the fluxes F and G by

$$A = \frac{\partial F}{\partial h_x}, \qquad B = \frac{\partial F}{\partial h} + \frac{\partial G}{\partial Y}, \qquad C = -\frac{\partial G}{\partial h_x}\frac{\partial F}{\partial Y}, \qquad D = \frac{\partial G}{\partial h}\frac{\partial F}{\partial Y} - \frac{\partial G}{\partial Y}\frac{\partial F}{\partial h}, \tag{49}$$

all evaluated at $h = h_0$, $Y = Y_0$, and $h_x = 0$.

Unstable modes k correspond to a positive real part of the growth rate $Re[\sigma]$, and marginally stable wavenumbers are obtained when $Re[\sigma] = 0$. Equation (48) gives marginal stability only at $k = 0$, which means that any unstable (or stable) solutions will be unstable (or stable) for all wavenumbers k. In the limit of large k, (48) gives two roots $\sigma_{1,2}$ with leading order real parts given by

$$Re[\sigma_1] = -Ak^2 + O(1), \qquad Re[\sigma_2] = \frac{C^2 - ABC - A^2B}{A^3} + O(k^{-1}). \tag{50}$$

The algebra for this problem is significantly simplified if we consider the limit of large Γ, and expand the coefficients in powers of $1/\Gamma$. For ease of notation we also define the quantity $\Theta_0 = h_0 - Y_0$. To leading order in $1/\Gamma$, we find that $A = [h_0^3 - \Theta_0^3]/3 > 0$, and

$$\frac{C^2 - ABC - A^2B}{A^3} = \frac{3h_0^3\Theta_0^3\left(h_0 - \Theta_0\right)^4\left(h_0 + 2\Theta_0\right)^2 S^2}{4\left(h_0^3 - \Theta_0^3\right)^3} > 0. \tag{51}$$

Therefore, in the limit of large Γ, the first root σ_1 has a negative real part, with a magnitude that grows like k^2. However, the second root σ_2 has a positive real part, that is a constant to leading order for large values of k. We can also show that for small k the unstable mode grows like k^2, and then increases monotonically to this constant value for large k. The system is therefore unstable to perturbations of any wavenumber. For parameter settings relevant to the full slump problem, the positive growth rate is typically extremely small in magnitude.

We have also shown numerically that this behaviour is generic for arbitrary values of Γ: that is, there is always one negative root that decays like k^2, and one positive root that grows monotonically from zero at $k = 0$ to a (typically very small) constant for large k. Therefore all wavenumbers are unstable. An example of the two roots is plotted in figure $7(b)$.

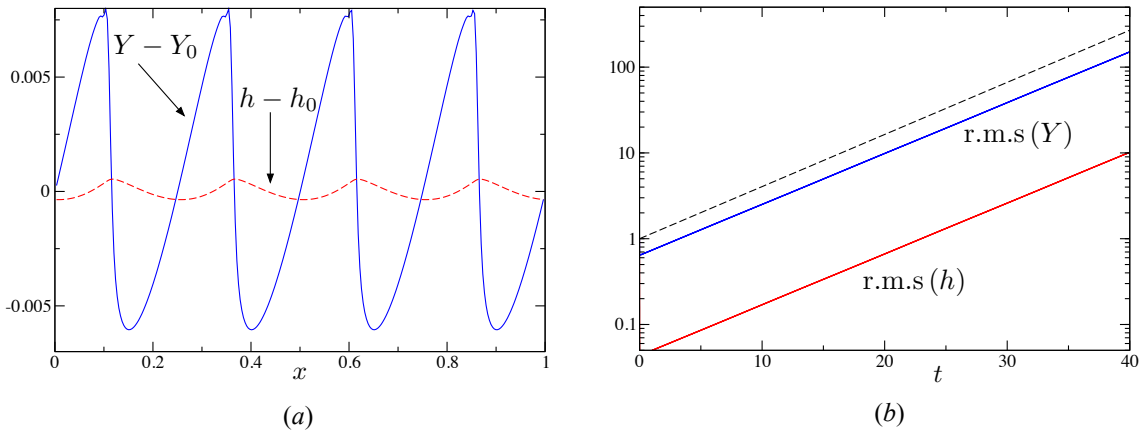

Figure 8: Numerical stability results for an initial perturbation of amplitude 10^{-5} and wavenumber $k = 8\pi$, for $\Gamma = 20$, $\beta = 0.95$, $S = 2$, $h_0 = 1$, and $Y_0 = 0.25$: (a) the perturbations to the yield surface $Y - Y_0$ (blue, solid) and to the height $h - h_0$ (red, dashed), at time $t = 50$, showing the formation of shocks in the yield surface; and (b) the measured root-mean-squared yield surface (blue) and height (red), scaled by the initial perturbation amplitude, and compared to the theoretical unstable growth rate $\left|e^{\sigma t}\right|$ (dashed) for large k, calculated from (50).

5.2 Numerical stability analysis

We can simulate the setup shown in figure 7(a) directly, with periodic boundary conditions in the x-direction. The height h and the yield surface Y are both subjected to the same small single-mode perturbation, which then evolves according to (41). Figure 8 shows the results of such a simulation, for an initial perturbation with wavenumber $k = 8\pi$, corresponding to 4 waves. The resulting perturbation to the height and to the yield surface (figure 8a) are observed to grow extremely slowly in comparison with the advection time of the background velocity. The instability is more prominent on the yield surface than on the height of the current. In the non-linear regime, the instability appears to lead to the formation of shocks on the material yield surface, with the same wavenumber as the original perturbation. We find that these shocks drive the initiation of high wavenumber oscillations, and this behaviour is perhaps a feature of our numerical scheme. The corresponding deformation of the height of the current takes the form of travelling waves. The measured amplitude of the perturbations gives the same growth rate as the theoretical prediction (50) for large k (figure 8b).

The analysis of this section shows that the idealised system is unstable to an interfacial instability at all wavenumbers, in the regions where the yield surface is a material curve. This result has important implications for our numerical simulations of the full slump problem, as instabilities with length scales down to the gird scale might be expected to form, and the results will likely vary with the spatial resolution of the computation. However, it should be remembered that the full system is not periodic in x, but rather the material part of the yield surface is bounded at each end by either critical or absolute stress contours, which limit the development and propagation of the instability. Furthermore, because the

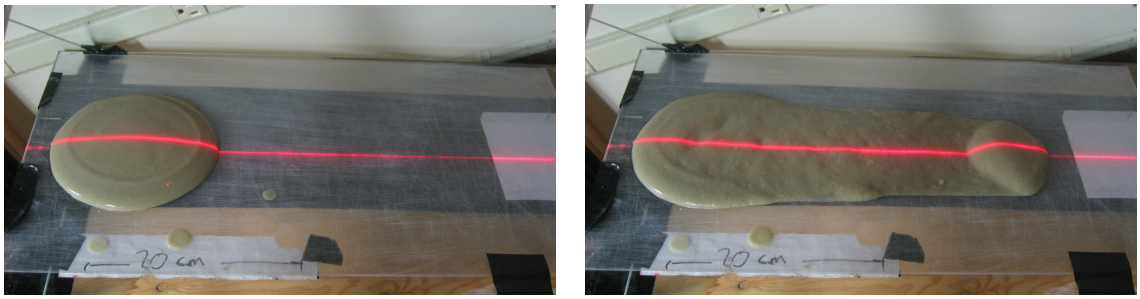

(*a*) (*b*)

Figure 9: Snapshots of a typical experiment in progress, with 10% by volume bentonite solution, $T_{\text{age}} = 240$ minutes, and an angle of 20°: (*a*) after $t = 5$ seconds; (*b*) after $t = 50$ seconds. For scale, the tattered white paper below the sample in each picture is 20 cm long.

growth rate is (typically) extremely small, the background advection of the flow is much faster than the growth of instabilities, and we expect them to be rapidly transported along the yield surface until they reach one of the stress contours. This behaviour is observed in the numerical results of section 4, where the instabilities are typically quashed by the absolute or critical stress contours before they significantly destabilise the flow and cause any noticeable deformation to the height $z = h$ of the current. It should, however, be noted that this is not always the case: particularly at smaller values of Γ and larger values of β, we find that instabilities on the yield surface can result in wave generation and deformation of the height of the current.

6 Experimental results

We have carried out a series of experiments to compare with the numerical simulations of our model. Our experimental setup consisted of a $\approx 1\,\text{m}^2$ glass plate, which was hinged at one end, and could be tilted and held at a desired angle using a pulley system. The plate was joined to a frame, which allowed for a laser pointer and a camera to be held in the same frame of reference as the plate. Samples of fluid were placed on the plate, which was then lifted to a given angle (details of the preparation of the fluid and the initialisation of the experiment are discussed below). A laser line was projected onto the fluid surface from directly above, facing down the slope, which allowed for measurements of the height of the current along the midplane (see figure 9 for typical photographs of the system during an experiment).

We performed experiments with two different thixotropic fluids: bentonite clay solution (10% by volume, *Quik-Gel* sodium bentonite, *Baroid drilling fluids*), and tomato ketchup (*Heinz*). Each of these fluids have been observed to exhibit thixotropy [6, 18]: in particular, there have been a variety of rheological measurements of bentonite [11, 19], which suggest that it exhibits many of the features of our rapid-transit rheological model (section 2). In order to ensure reproducibility in the results, all the fluid samples were initially subjected to vigorous shear for at least 30 minutes. This shear was intended to remove any initial

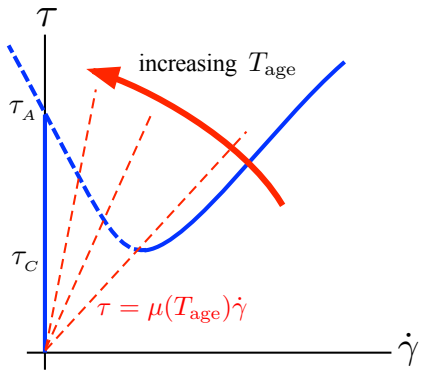

Figure 10: Schematic of the steady-state constitutive relationship (thick blue), as in figure 2, together with the local linear relationship between τ and $\dot{\gamma}$ for increasing ageing times T_{age} as marked (thin red dashed). The time-dependent 'effective yield stress', above which the fluid de-structures, is given by the intersection between the curves. For $T_{\text{age}} = 0$, the effective yield stress is equal to the critical stress $\tau_{_C}$, and there is no hysteresis in the system. As $T_{\text{age}} \to \infty$, the effective yield stress tends towards the absolute stress $\tau_{_A}$, and $\lambda \to 1$.

structure in the fluid. A fixed volume (150 ml) of the fluid was then slumped on a horizontal plate, by pouring into a hollow cylindrical (5 cm radius) mould, which was then lifted. In this way, the fluid attained its rest state on a flat plate, which corresponds to the initial condition of the numerical simulations (section 4). Samples were then left to age for different periods of time T_{age}. During this time, the samples were kept under airtight covers to limit the effects of evaporation. The substrate for the experiments was made of sanded perspex, in order to avid any slip at the base of the current. There is an important phenomenological distinction between this 'genuine' slip, in which the whole fluid column slides on the substrate, and the apparent slipping of structured fluid which is actually due to lubrication from a de-structured layer at the base of the current. The latter effect, which results in a thin layer of fluid being left behind on the substrate, is consistent with the theoretical 'no-slip' boundary condition on the base of the current (10), and was observed in many of our experiments.

Before presenting our experimental results, we briefly consider how we expect the behaviour of the fluid to vary with different ageing times T_{age}, based on the theoretical model that was discussed in section 2. While the fluid sample is at rest, the structure should evolve according to (2), with $\dot{\gamma} = \boldsymbol{u} = 0$: *i.e.*

$$\frac{\partial \lambda}{\partial t} = \frac{1-\lambda}{T}. \tag{52}$$

For a given ageing time T_{age}, there is a corresponding value of λ, given by (52). This value of λ corresponds to a viscosity, $\mu(\lambda)$, and thus to a linear constitutive relationship $\tau = \mu(\lambda)\dot{\gamma}$. The local value of the stress at which the fluid becomes de-structured (the 'effective yield stress') is then given by the intersection between this linear constitutive relationship and the steady state hysteresis loop (shown schematically in figure 10). If the ageing time T_{age} is small, this effective yield stress will be very close to the critical stress $\tau_{_C}$,

and we would therefore expect the sample to behave rather like a simple yield-stress fluid. As $T_{\rm age}$ increases, the sample should increasingly exhibit the features that we observed in our numerical simulations (section 4), as the effective yield stress increases towards $\tau_{_A}$, and the extent of hysteresis in the system increases. Moreover, the discontinuity in $\dot{\gamma}$ at the effective yield stress will also increase with $T_{\rm age}$, and the system should exhibit increasingly dramatic 'avalanche' behaviour.

6.1 Bentonite

We examined the behaviour of different bentonite solutions with filtered water: 7.5%, 10%, and 12.5% bentonite by volume. The 12.5% solution was very viscous, and so suffered from slipping on the substrate, while the 7.5% solution had a relatively low viscosity, which appeared to result in some inertial effects, and caused the fluid to flow too rapidly for accurate measurements. Here, therefore, results are presented only for the 10% bentonite solution.

Figure 11 shows measurements of the height profiles over time, for different ageing times $T_{\rm age}$, at a fixed angle of 20°. Figure 12 shows the height profiles at different ageing times for a slightly larger inclination angle of 24°. As a comparison, we also carried out some experiments with a 'joint compound' solution (*Sheetrock* all-purpose joint compound), which, over the timescale of an experiment, appeared very like an ideal yield-stress fluid. Measurements of the height of the joint compound are shown in figure 11(a).

These measurements show that the behaviour of bentonite is strongly dependent upon the ageing time. Consider, for example, the results on a 20° slope (figures 11b-d). For very small ageing times, the behaviour is similar to the joint compound (yield-stress fluid, figure 11a), although the formation of a nose at the front of the downward-moving current is more pronounced: there is no raised 'horseshoe' at the back of the current, and the fluid evolves rapidly after the experiment starts. However, as the ageing time $T_{\rm age}$ increases, the samples display behaviour that is more similar to the numerical simulations of section 4: there is an increasingly pronounced residual 'horseshoe' of fluid left behind at the back of the current, and the thinnest part of the current for late times is in the middle, between the horseshoe and the nose. These features are even more striking if the slope is increased by 4° (figure 12). Here, the sample thins very dramatically in the interior, which results in an extremely pronounced nose at the head of the current and residual horseshoe at the rear. This behaviour is more dramatic than is predicted by the theoretical model, possibly because of the destructuring effects of extensional stresses in the current, which the model does not take into account. This issue is discussed in section 7. It is important to highlight that, even in the most extreme examples (e.g. figure 12c), the nose did not appear to be slipping on the substrate as it moved down the slope, but rather there was always a thin lubricating layer of de-structured fluid along the base.

Figure 13(a) shows the final position of the nose of the current, $x_{_F}$, as a function of the inclination angle, for different ageing times $T_{\rm age}$. As discussed above, we anticipate that for larger ageing times, the stress (and hence the angle) at which the fluid de-structures (and evolves to the small-λ stable branch of the constitutive relationship), should increase, and the corresponding flow after de-structuring should be increasingly dramatic (as the value of $\dot{\gamma}$ on the small-λ stable branch will be larger). Both of these features can be observed in

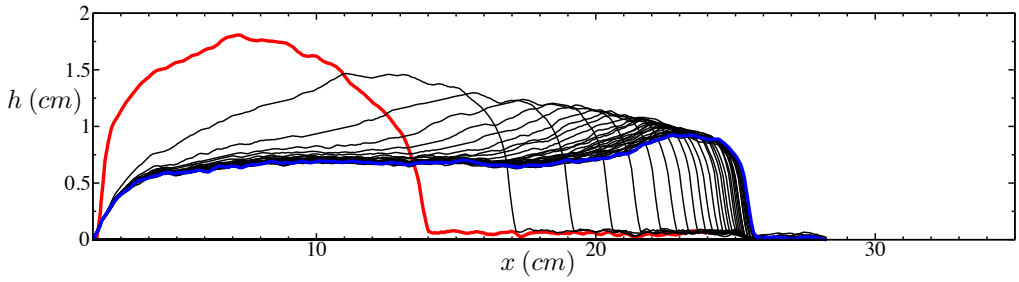

(*a*) Joint compound, 34°

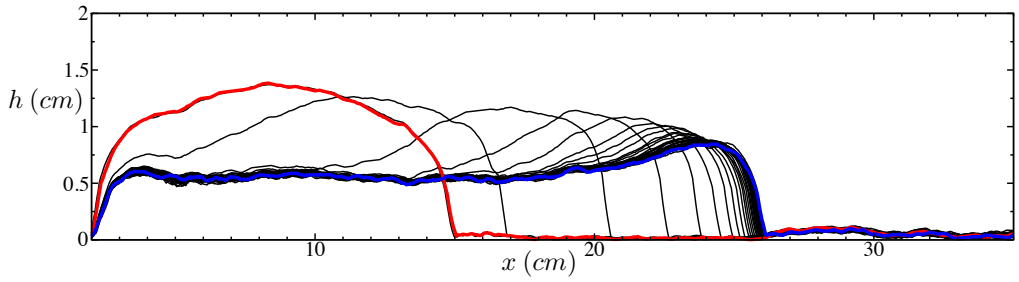

(*b*) $T_{\text{age}} = 5$ minutes

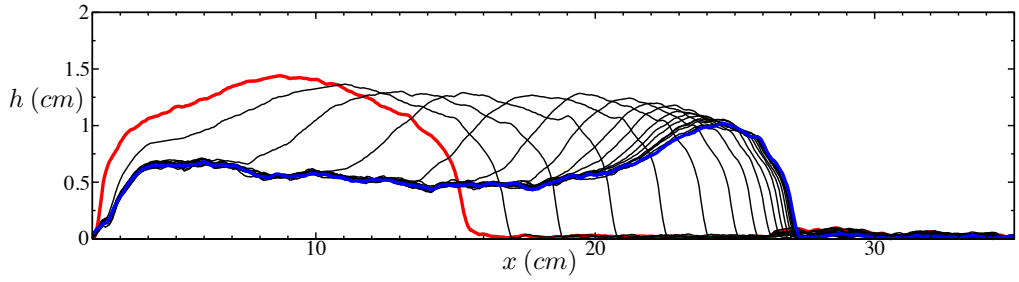

(*c*) $T_{\text{age}} = 60$ minutes

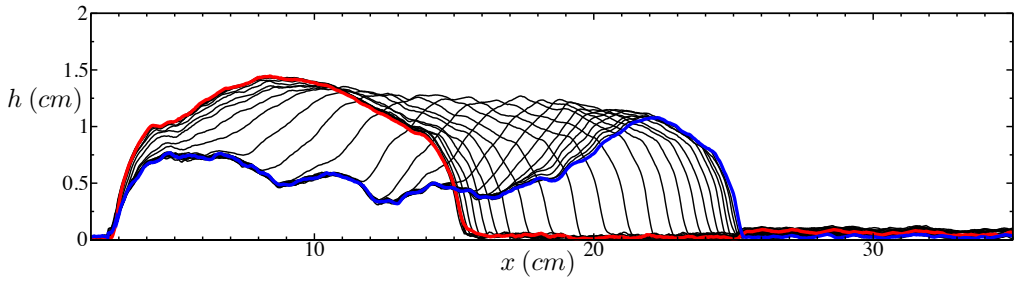

(*d*) $T_{\text{age}} = 240$ minutes

Figure 11: Snapshots of the height of the midplane over time, measured using a laser line, for (a) a joint compound solution on a 34° slope, which behaves very like an ideal yield-stress fluid [14, 17], and for (b) – (d) 10% (by volume) bentonite solution on a 20° slope, for different ageing times T_{age} as marked. The x axis gives the distance from the back of the current. Lines are plotted every ≈ 2 seconds, except in (b), where lines are plotted every ≈ 0.5 seconds. Red and blue lines signify the initial and final profiles, respectively. As T_{age} increases, the response of the bentonite increasingly differs from the ideal yield-stress behaviour in (a), as discussed in the text, and in the caption to figure 12.

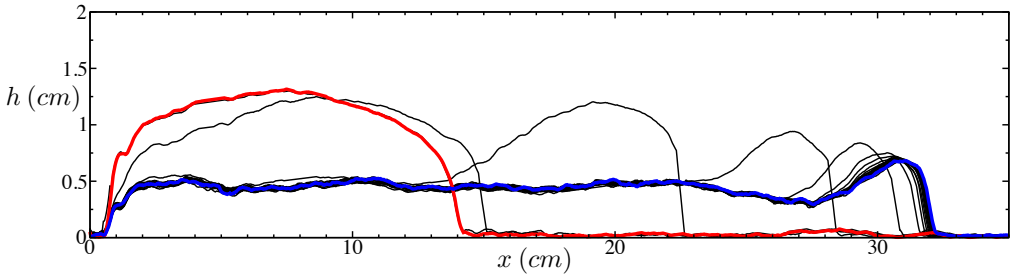

(*a*) $T_{\text{age}} = 5$ minutes

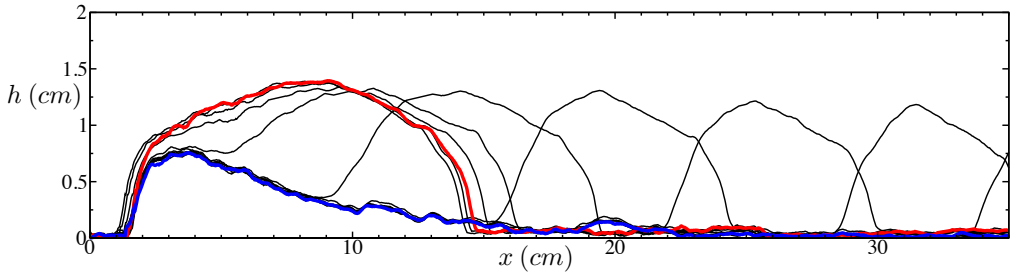

(*b*) $T_{\text{age}} = 240$ minutes

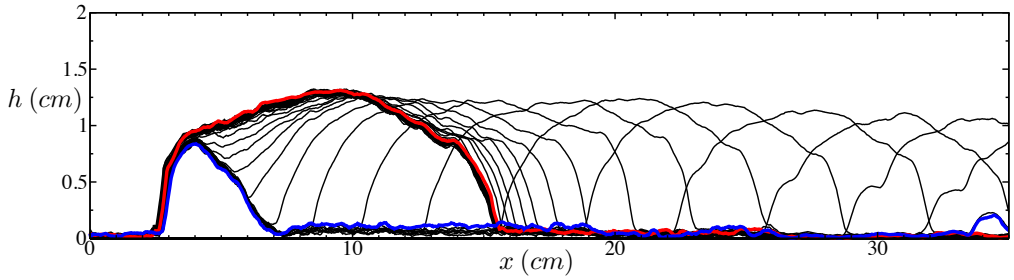

(*c*) $T_{\text{age}} = 1080$ minutes

Figure 12: Snapshots of the height of the midplane over time for 10% (by volume) bentonite solution on a 24° slope, for different ageing times T_{age} as marked.. Lines are plotted every ≈ 2 seconds, except in (a), where lines are plotted every ≈ 0.5 seconds. Red and blue lines signify the initial and final profiles, respectively. In (b) and (c), the nose of the current eventually moves off the end of the plate. For the larger values of T_{age}, the same qualitative features that were observed in the numerical results (section 4) can be seen: the back of the current remains fixed (the 'horseshoe'), and there is a 'nose' of fluid which moves rapidly down the slope. The sample in (d), which is aged for 1080 minutes, does not move on a 20° slope, which exemplifies the increasingly dramatic 'avalanche' behaviour of the fluid for large T_{age}.

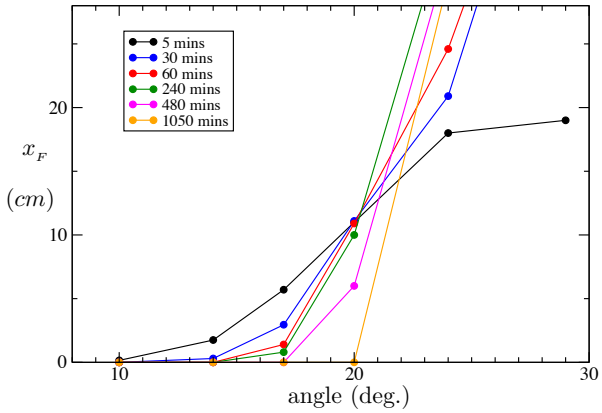

(*a*) final nose distance

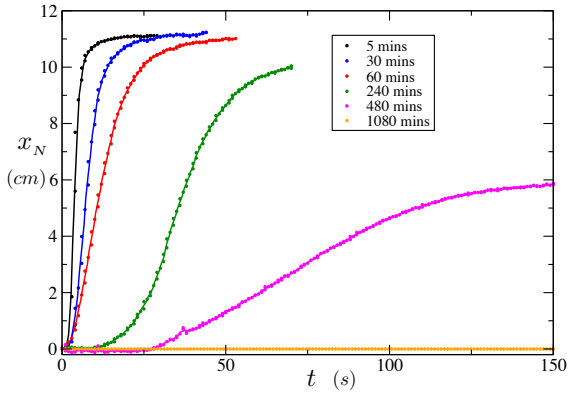

(*b*) 20° slope

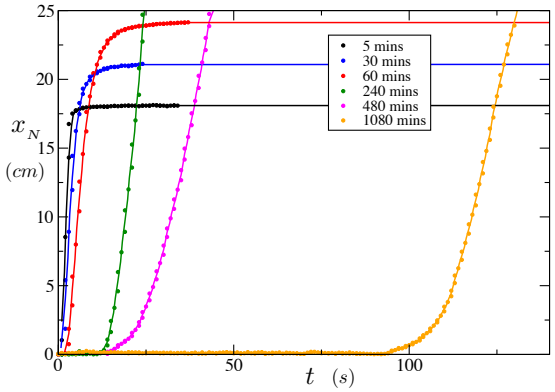

(*c*) 24° slope

Figure 13: Position of the nose of the current for 10% (by volume) bentonite solution: (*a*) the final distance travelled by the nose x_F, for different ageing times T_{age}, showing the increasingly narrow band of angles over which the de-structuring of the fluid becomes more dramatic; (*b*) the distance travelled by the nose $x_N(t)$ on a 20° slope; and (*c*) the distance travelled by the nose $x_N(t)$ on a 24° slope. Notice the change in curvature of the lines in (*b*) and (*c*) for longer ageing times. Measurements which appear above the top of the graph signify that the current reached the end of the plate.

figure 13(a): for small values of $T_{\rm age}$, the final distance of the nose $x_{_F}$ steadily increases with the angle of inclination, while for larger $T_{\rm age}$, there is an increasingly thin band of angles over which $x_{_F}$ changes dramatically. This 'avalanche' behaviour is most clearly observed in the samples that were left to age for $T_{\rm age} = 1080$ minutes, where the fluid remains stationary on a 20° slope, but fails dramatically and flows off the bottom of the plate at 24°.

The transient behaviour of the nose of the current $x_{_N}(t)$ is shown for two different angles in figures 13(b) and (c), again for different values of $T_{\rm age}$. These figures reveal a change in the evolution of the current for larger ageing times. For small values of $T_{\rm age}$, the nose of the current moves most rapidly at $t = 0$, as in the case of an ideal yield-stress fluid. However, as $T_{\rm age}$ increases the nose of the current takes increasingly long to move, and then gradually accelerates. This behaviour agrees with previous observations made by Coussot *et al.* [10]. We anticipate that this slow acceleration is a result of the gradual breakdown of structure in the fluid, which mathematically corresponds to the slow evolution of the structure parameter λ towards the steady state, as modelled by time derivative in (2). This behaviour is not, therefore, captured by the rapid-transit model, and thus is not observed in our numerical results.

Figures 13(b) and (c) also show that the current comes to an abrupt halt after flowing down the plane. The shape of this final profile is much like the profile during the flow: the immobile current has a clear raised horseshoe at the back and a raised nose at the front. This behaviour is quite unlike that predicted by the numerical simulations (section 4.2.2), which suggest that the flow should slowly evolve towards a final profile that is approximately flat. The reasons for this difference are unclear.

6.2 Ketchup

We have also carried out experiments using Heinz tomato ketchup. Ketchup is an interesting and complex multicomponent fluid, and is difficult to use experimentally due to its tendency to separate over time. In particular, ketchup readily expels vinegar, which gathers around the base of the sample if it is left at rest for more than a few minutes. Despite these difficulties, which suggest caution is needed in analysing these results, it is still possible to observe clear thixotropic behaviour, and to draw qualitative comparisons both with the measurements for bentonite and with our theoretical model. While we gathered a range of measurements using ketchup, we will only briefly discuss the qualitative behaviour here, because of this separation problem.

Figure 14 shows snapshots of the height of the current over time, for different ageing times $T_{\rm age}$. Although the dependence on $T_{\rm age}$ seems much less dramatic than with bentonite (figure 11), we still observe the development of a structured horseshoe of fluid at the rear of the current for large ageing times, which is absent for smaller ageing times. We found that ketchup does not exhibit the same catastrophic failure at a particular angle that we observed in fully structured bentonite (e.g. figure 12c), except at much larger angles, when the fluid starts to slip on the base (see the discussion of slip above), so that the nature of the experiment changes.

A photograph of the ketchup current (figure 15a) shows the structured horseshoe remnant, and the gravity current extruding down the slope. This picture highlights the complex structure of the surface of the current: the evident surface structure is perhaps the result

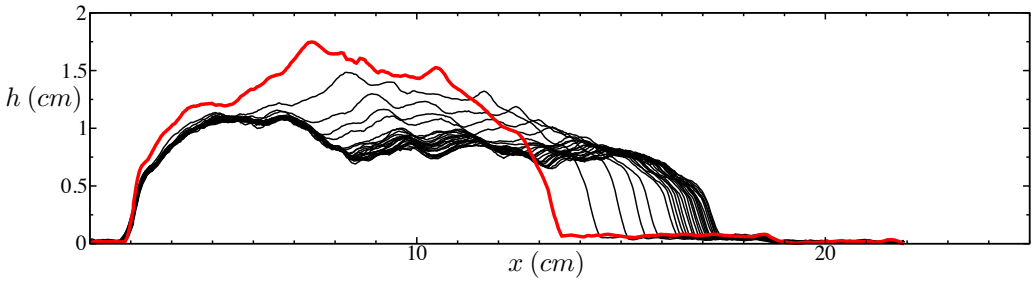

(*a*) $T_{\text{age}} = 5$ minutes

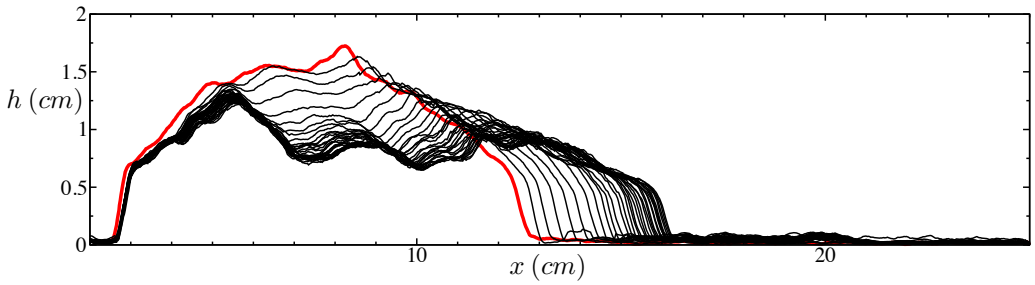

(*b*) $T_{\text{age}} = 240$ minutes

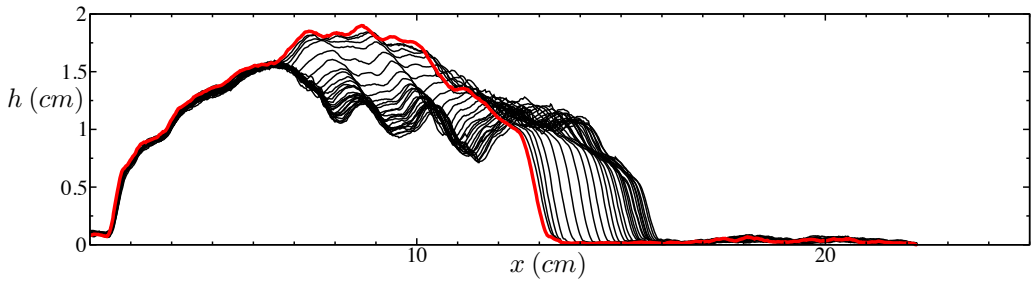

(*c*) $T_{\text{age}} = 1080$ minutes

Figure 14: Snapshots of the height of the midplane over time for Heinz tomato ketchup on a 14° slope, for different ageing times T_{age} as marked.. Lines are plotted every ≈ 10 seconds. Red lines signify the initial profiles: in contrast to bentonite, the samples continue to move slowly down the slope for very long times, and thus the final position of the slump is not necessarily attained. For larger values of T_{age} there is a clear structured horseshoe at the rear of the current.

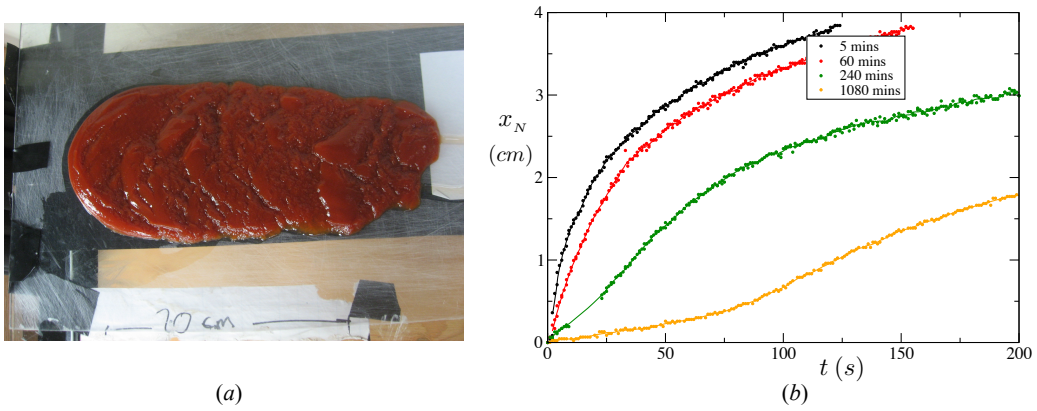

(a) (b)

Figure 15: Results with Heinz tomato ketchup: (a) a photograph from above of a ketchup current after an experiment (downslope is to the right), showing a structured horseshoe at the back (left), and significant surface texture on the rest of the current; and (b) the evolution of the nose of the current $x_N(t)$ on a 14° slope, showing the same change in curvature that was observed with bentonite (figure 13b and c). Unlike bentonite, the current continued to flow throughout the experiment, rather than coming to a halt.

of an instability, such as the interfacial instability that was analysed in section 5.

Figure 15(b) shows the evolution of the position of the nose $x_N(t)$ for different values of T_{age}. As in the case of bentonite (figure 13b and c), the current gradually accelerates for longer ageing times, in contrast to the behaviour at small values of T_{age}. Interestingly, the ketchup current continued to flow throughout the experiment, rather than coming to an abrupt halt like the bentonite.

7 Conclusions

As discussed in section 1, despite a range of rheological studies of thixotropy there has been relatively little work that couples the rheology to the flow in a physical system. In this report we have presented and discussed a rheological model for thixotropic fluids, and applied it in the context of gravity-driven flow on a slope. We modelled this system both numerically and experimentally, and, despite some intriguing differences, on the whole we found broad qualitative agreement between the results.

In section 2, we presented a rheological model that we use to describe the effects of thixotropy. This model is based on a selection of previous models (e.g. [11, 19]), but also includes the concept of an *absolute stress* τ_A, above which even fully structured fluid will de-structure and begin to flow. In addition, based on previous empirical observations [1, 7, 11, 20], we introduced the simplifying 'rapid-transit' approximation, which assumes that λ evolves instantaneously to its steady-state value.

In sections 3 and 4, we applied our rapid-transit rheological model to the problem of a finite shallow current on a slope, and presented numerical results of the flow in two and three dimensions. For these theoretical results, we assumed that the fluid was initially fully structured. We found that the flow is characterized by a raised 'horseshoe' of structured

fluid at the back of the current, in agreement with previous experimental observations [10]. The model also shows that there is a critical angle, above which the current will flow (in some cases, dramatically), and below which the current will not move.

Motivated by the presence of high-wavenumber fluctuations in these numerical results, in section 5 we explored the stability of an idealised shallow-layer system. We found that the internal interface (yield surface) between the structured and de-structured fluid is always weakly unstable to perturbations at any wavelength. Within this idealised system, we numerically followed the instability into the non-linear regime, and found that the instability develops into travelling shocks on the material part of the yield surface. However, the growth rate of the instability is typically extremely small compared to the rate of propagation of the current, and, in the full (non-idealised) system, the material part of the yield surface is always bounded by a constant stress contour at either end, which damp any oscillations. On the whole, therefore, this instability does not appear to have a significant effect on the propagating current.

Finally, in section 6, we presented experimental results of the same shallow-layer inclined system, with two thixotropic fluids: bentonite clay solution, and tomato ketchup. We observed that, as the ageing time T_{age} increased, the bentonite solution evolved in qualitative agreement with the theoretical predictions: from simple yield-stress-fluid behaviour for small T_{age}, to increasingly dramatic 'avalanche' behaviour for larger T_{age}. The shape of the current for larger T_{age} is similar to that predicted by the numerical simulations: a notable structured horseshoe of fluid at the back of the current; a thinner region in the interior; and a nose at the front. However, unlike the numerical predictions, which suggest that the current should evolve slowly to a relatively flat final profile, the bentonite always came to an abrupt halt after flowing some way down the plane, leaving a pronounced horseshoe and nose at the back and front of the current respectively. The reasons for this different behaviour are not clear, although perhaps the neglect of extensional stresses in the theoretical model could be relevant (see the discussion below).

The results for ketchup are more difficult to analyse, due to the material separating into its constituent fluid components. However, we again observe that the shape of the current increasingly resembles the numerical solutions for larger ageing times, with a structured horseshoe at the back of the current. The ketchup current also undergoes an instability or deformation of the free surface as it flows down the slope, which may be related to the instability process in the theoretical model (section 5). The evolution of the nose of the current for both ketchup and bentonite solution undergoes a qualitative change for different values of T_{age} (as in [10]), from initial gradual deceleration for small T_{age}, to initial gradual acceleration for larger T_{age}. This behaviour is not captured by the numerical results, presumably because of the rapid-transit approximation.

While many of the main phenomenological features of the experimental results agree well with both the numerical and theoretical models, we find that bentonite can undergo even more dramatic de-structuring than the numerical solutions suggest. This difference is perhaps due to the details of the rheological model, in which, for example, the viscosity may have a more sensitive dependence on the strain rate. However, the difference could also be explained by the neglect of extensional stresses from the theoretical shallow-layer model (section 3). Flow in a de-structured layer may induce significant extensional stresses in the structured (and therefore much more viscous) layer above, which are not included in the

model. If the upper layer is sufficiently viscous, these extensional stresses can contribute to the stress invariant τ at the same order of ε as the shear stress. The inclusion of extensional stresses would lead to more of the current becoming de-structured, which would result in an increased thinning of the interior of the current, as is observed experimentally. It has proved somewhat complicated to develop a consistent model that incorporates extensional and shear stresses throughout the current, and this remains an intriguing avenue for further study.

Acknowledgments

A great many thanks are due to the directors, staff, principal lecturers, and administrators of the 2012 WHOI GFD summer program, and to all who came and went from Walsh cottage during the program. I would particularly like to thank Neil Balmforth, both for suggesting this project, and for countless helpful and stimulating discussions. His interest and input have been invaluable in this work. I would also like to thank Colm Caulfield for his kind encouragement during and prior to this summer, and Anders Jensen for his assistance with the experimental work. Finally, I am extremely grateful to all the other fellows for contributing to such an interesting, inspiring and enjoyable summer.

References

[1] A. Alexandrou, N. Constantinou, and G. Georgiou, *Shear rejuvanation, aging and shear banding in yield stress fluids*, J. Non-Newtonian Fluid Mech., 158 (2009), pp. 6–17.

[2] N. Balmforth and R. Craster, *A consistent thin-layer theory for Bingham plastics*, J. Non-Newtonian Fluid Mech., 84 (1999), pp. 65–81.

[3] ——, *Geomorphological Fluid Mechanics*, Springer, 2001, ch. Geophysical aspects of Non-Newtonian fluid mechanics.

[4] N. Balmforth, R. Craster, and R. Sassi, *Shallow viscoplastic flow on an inclined plane*, J. Fluid Mech., 470 (2002), pp. 1–29.

[5] N. Balmforth, R. Craster, and C. Toniolo, *Interfacial instability in non-Newtonian fluid layers*, Phys. fluids, 15 (2003), pp. 3370–3384.

[6] H. Barnes, *Thixotropy — a review*, J. Non-Newtonian Fluid Mech., 70 (1997), pp. 1–33.

[7] D. Bonn, H. Tanaka, P. Coussot, and J. Meunier, *Ageing, shear rejuvenation and avalanches in soft glassy materials*, J. Phys.: Condens. Matter, 16 (2004), pp. S4987–S4992.

[8] H. Chanson, S. Jarny, and P. Coussot, *Dam break wave of thixotropic fluid*, J. Hydr. Eng., 132 (2006), p. 280.

[9] K. Chen, *Wave formation in the gravity-driven low Reynolds number flow of two liquid films down an inclined plane*, Phys. Fluids A, 5 (1993), p. 3038.

[10] P. Coussot, Q. Nguyen, H. Huynh, and D. Bonn, *Avalanche behaviour in yield stress fluids*, Phys. Rev. Lett., 88 (2002), p. 175501.

[11] ——, *Viscosity bifurcation in thixotropic, yielding fluids*, J. Rheol., 46 (2002), pp. 573–589.

[12] F. Da Cruz, F. Chevoir, D. Bonn, and P. Coussot, *Viscosity bifurcation in granular materials, foams, and emulsions*, Phys. Rev. E, 66 (2002), p. 051305.

[13] P. de Souza Mendes, *Modelling the thixotropic behavior of structured fluids*, J. Non-Newtonian Fluid Mech., 164 (2009), pp. 66–75.

[14] A. Hogg and G. Matson, *Slumps of viscoplastic fluids on slopes*, J. Non-Newtonian Fluid Mech., 158 (2009), pp. 101–112.

[15] H. Huppert, *The propagation of two-dimensional and axisymmetric viscous gravity currents over a rigid horizontal surface*, J. Fluid Mech., 121 (1982), pp. 43–58.

[16] J. Lister, *Viscous flows down an inclined plane from point and line sources*, J. Fluid Mech., 242 (1992), pp. 631–653.

[17] K. Liu and C. Mei, *Slow spreading of a sheet of Bingham fluid on an inclined plane*, J. Fluid Mech., 207 (1989), pp. 505–529.

[18] J. Mewis, *Thixotropy*, Adv. Colloid Interface Sci., 147-148 (2009), pp. 214–227.

[19] P. Moller, A. Fall, V. Chikkadi, D. Derks, and D. Bonn, *An attempt to categorize yield stress fluid behaviour*, Phil. Trans. R. Soc. A, 367 (2009), pp. 5139–5155.

[20] P. Moller, J. Mewis, and D. Bonn, *Yield stress and thixotropy: on the difficulty of measuring yield stress in practice*, Soft Matter, 2 (2006), pp. 274–283.

[21] A. Putz and T. Burghelea, *The solid-fluid transition in a yield stress shear thinning physical gel*, Rheol. Acta, 48 (2009), pp. 673–689.